Biomaterials
Science

PAPER

View Article Online
View Journal | View Issue

Cite this: *Biomater. Sci.*, 2025, **13**, 3689

Borax - and tannic acid-based post-3D-printing treatment to tune the mechanical properties of scaffolds†

Julia Simińska-Stanny,‡[a] Parinaz Hobbi,‡[a] Pejman Ghaffari-Bohlouli,[a] Man Li,[a] Adam Junka,[b] Hafez Jafari,[a] Christine Delporte,[c] Lei Nie[d] and Armin Shavandi*[a]

Received 30th January 2025,
Accepted 28th April 2025

DOI: 10.1039/d5bm00151j

rsc.li/biomaterials-science

Digital light processing (DLP) methods are constrained by the narrow range of cell-compatible resins, limiting their use in biomedical applications that require varied mechanical and biofunctional properties. Current bioresins based on natural polymers such as methacrylated gelatine or alginate usually lack sufficient stretchability and toughness. In this study, we propose a post-processing strategy to tune the mechanical and functional properties of a DLP printable polyethylene glycol diacrylate (PEGDA)/polyvinyl alcohol (PVA) resin *via* simple treatment with 5% (w/v) tannic acid (TA) or borax (B). The TA treatment reduced the resin's toughness by ∼17% and compressive modulus by ∼16%, while B treatment increased the toughness by ∼53% and the compressive modulus by ∼44% compared with non-treated hydrogels. TA-treated hydrogels continuously released over 59% of the loaded TA, demonstrating antibacterial and radical scavenging activities. Moreover, TA-treated hydrogels, DLP-printed in a tubular shape, demonstrated the highest durability, remaining intact for ∼32 cycles before failure, which was ∼17 cycles more than that for the non-treated hydrogels. Our *in vivo* larval model further confirmed the hydrogels' biocompatibility. This study offers a practical approach for post-fabrication tuning of the mechanical and bioactive properties of DLP-printed PEGDA-PVA hydrogels, expanding the utility of existing resins for potential biomedical applications, such as soft tissue engineering.

1. Introduction

Photocurable 3D printing technology surpasses extrusion-based 3D printing in terms of material versatility, print speed, and reproducibility.[1] Even low-light-intensity (15 mW cm^{-2}) commercial DLP 3D printers have the advantage of being able to achieve high-resolution complex structures (100 μm)[2] compared with multiple extrusion 3D printers using nozzles with nominal diameters of >250 μm and lower resolution.

However a significant limitation of DLP printing for the tissue engineering sector is the narrow selection of biocompatible resins and photoinitiators and achieving sufficient stretchability and toughness.[3] Only few materials, such as gelatin methacrylate (GelMA),[4] silk fibroin, chitosan methacrylate, PEGDA,[5] κ-carrageenan,[6] hyaluronic acid methacrylate,[7] and norbornene,[8] have been successfully used for DLP bioprinting in biomaterials engineering. Among these, PEGDA excels owing to its rapid and efficient photocrosslinking capabilities.

In contrast, GelMA and methacrylated silk fibroin (SilMA), although biocompatible, often require higher polymer concentrations (GelMA = 13%–15% w/v;[9,10] methacrylated silk fibroin ≈ 30% w/v[11]) than PEGDA (∼5%–10% w/v) or longer crosslinking times (>1 min; PEGDA typically required <30 s) owing to their limited number of crosslinkable moieties. This can result in reduced resolution, limiting their versatility for high-resolution DLP bioprinting applications.[12]

DLP printing requires precise control of various fabrication parameters, such as the light intensity and step height.[2]

---

[a] 3BIO-BioMatter, Université libre de Bruxelles (ULB), École Polytechnique de Bruxelles, Avenue F.D. Roosevelt, 50 – CP 165/61, 1050 Brussels, Belgium. E-mail: armin.shavandi@ulb.be
[b] P.U.M.A., Platform for Unique Model Application, Department of Pharmaceutical Microbiology and Parasitology, Wroclaw Medical University, Borowska 211a, 50-556 Wroclaw, Poland
[c] Laboratory of Pathophysiological and Nutritional Biochemistry, Faculté de Médecine, Université libre de Bruxelles (ULB), Campus Erasme – CP 611, Route de Lennik, 808, 1070 Bruxelles, Belgium
[d] College of Life Science, Xinyang Normal University, Xinyang, China

† Electronic supplementary information (ESI) available. See DOI: https://doi.org/10.1039/d5bm00151j

‡ These authors contributed equally to this work and should be considered as first coauthors.

Insufficient curing can lead to incomplete polymerization, while excessive curing can cause attachment issues. Achieving optimal crosslinking kinetics necessitates careful adjustment of resin viscosity, concentration of crosslinkable moieties, and the concentration of photoinitiators/photoabsorbers.[5]

Various polyethylene glycol (PEG) and PEG-acrylate hydrogels have been developed recently for biomedical applications, including for *in vivo* drug delivery[13] and wound healing.[14] However, their inherent brittleness limits their use in tissue engineering.[15]

To address the brittleness of low-molecular-weight (LMW) PEGDA (<2 kDa), researchers have formulated PVA/PEGDA resins,[16,17] and it has been found that PVA's hydrophilic and flexible nature can improve the material's mechanical properties.[18,19] 3D-printed PEGDA/PVA showed a self-healing capacity[20] and tunable swelling properties.[21] The mechanical properties of PVA hydrogels can be modified by creating PVA-borax (sodium tetraborate decahydrate) complexes. Borax (B), a boron-containing compound, can crosslink with polyols like PVA through the formation of borate-ester bonds. These bonds enhance the hydrogel's mechanical properties, including its elasticity, strength, and self-healing capabilities.[18] Moreover, the reversible nature of borate bonding allows for tunable mechanical properties, depending on the pH and concentration, and also supports network rearrangement under physiological conditions,[22] making borax a potential modifier for bioresin-based hydrogel scaffolds. PVA-borax hydrogels are easy to shape, have adjustable mechanical properties, and can adhere to multiple surfaces.[18]

Tannic acid (TA), a polyphenol molecule, has shown the ability to improve the physical properties of hydrogels owing to the abundant hydroxyl (OH) groups in its structure in the forms of catechol and pyrogallol.[23] The additional –OH groups serve as crosslinking motifs through hydrogen bonding, thereby facilitating the synthesis of hydrogels with enhanced strength and elasticity.[24] For example, Chen *et al.* showed that the incorporation of TA into the PEGDA hydrogel enhanced the hydrogel's toughness, stretchability, self-healing ability, and underwater adhesive properties.[25] Similarly, another study reported improved mechanical properties, bioadhesive strength, and antimicrobial activity in PVA/ascorbic acid hydrogels following treatment with TA.[26] Beyond its mechanical contributions, TA also offers biological functionality. Tannic acid is well known for its antioxidant, antibacterial, and anti-inflammatory properties, making it relevant for tissue engineering applications.[27] Thus, the incorporation of TA into the hydrogel structure can result in a bioactive hydrogel with antioxidant, antimicrobial, and anti-inflammatory properties, as well as an adhesion capability.[28]

In this study, we hypothesized that post-printing treatments with TA and borax may enhance the mechanical properties and bioactivity of the printed constructs by improving the flexibility, toughness, and adding functionalities, such as antimicrobial and free radical-scavenging activities.

2. Results and discussion

2.1 Rational design of the biomaterial resin

Commercial low molecular weight PEGDA (*e.g.*, 5 kDa) is known to be brittle when used in light-based fabrication methods.[29] Meanwhile, it is known that PVA's flexibility and hydrophilic nature can improve the mechanical properties and durability of the resulting structures.[30] Therefore, to enhance the flexibility of our PEGDA-based DLP-printed constructs, various amounts of PVA (1–3 vol%) were incorporated in the biomaterial resin formulations.

Several PEGDA-PVA biomaterial resins were prepared with varying concentrations of PEGDA (6%–10% wt/v) and PVA (1%–3% wt/v). These formulations were designated as PXPVAY, where X and Y represent the concentrations of PEGDA and PVA (% wt/v) (Fig. 1A). The viscoelastic properties of all these formulations were assessed by a rheometer after the photocrosslinking (Fig. 1B). All the prepared hydrogels exhibited a shear-thinning behavior, with the viscosity decreasing as the shear rate was increased from 0.01 to 100 1 s^{-1}. The hydrogel with the highest concentration of PEGDA (10% wt/v) and the lowest concentration of PVA (1% wt/v) (P10PVA1) showed the highest viscosity (Fig. 1B). This shows the importance of the PEGDA concentration on the structural integrity of the hydrogel due to its primary role in crosslinking. The hydrogel viscosity is a critical factor for DLP printing, as the resin, once crosslinked, needs to be stable enough to adhere to and hold on to the platform upside down for the rest of the printing process. Considering the hydrogel viscosity as a criterion for determining the mechanical strength, we selected two formulations (P8PVA3 and P10PVA1) with the highest and lowest content of PVA for further evaluation.

During the DLP-printing process (Fig. 1C), the build platform lowers to cure a layer of the material according to the design.[15] To ensure quick gap refilling between printing stages and maintain an adequate resin level for subsequent layer curing, the resin should exhibit flowability.[31] Although a higher viscosity can often enhance the structural integrity, it may hinder the DLP-printing process by limiting the resin flow.[2] Ideally, biomaterial-based resins should exhibit viscosities below 10 Pa s, and achieving this may require the addition of viscosity modifiers or solvents.[32] Successful DLP printing has been reported with resin viscosities as low as 0.93 Pa s at a shear rate of 10 s^{-1}.[33] In our work, the viscosities of the selected formulations (P8PVA3 and P10PVA1) (Fig. 1D) were both below 10 Pa s, falling within the recommended range for DLP printability.

Furthermore, amplitude sweep tests were performed on the P8PVA3 and P10PVA1 biomaterial resins and hydrogels (Fig. 1E). The results confirmed the dominance of the elastic behavior over the viscous behavior for both hydrogels within their linear viscoelastic region (LVR). P10PVA1 showed a storage modulus (G') of approximately 6000 Pa in the LVR and a critical strain of ∼3%, while P8PVA3 showed a G' of ∼1000 Pa and a critical strain of ∼22%. Based on these results, P8PVA3 was chosen as the superior formulation for DLP printing. Although P10PVA1 showed a higher G' in the LVR, P8PVA3 exhibited a higher critical

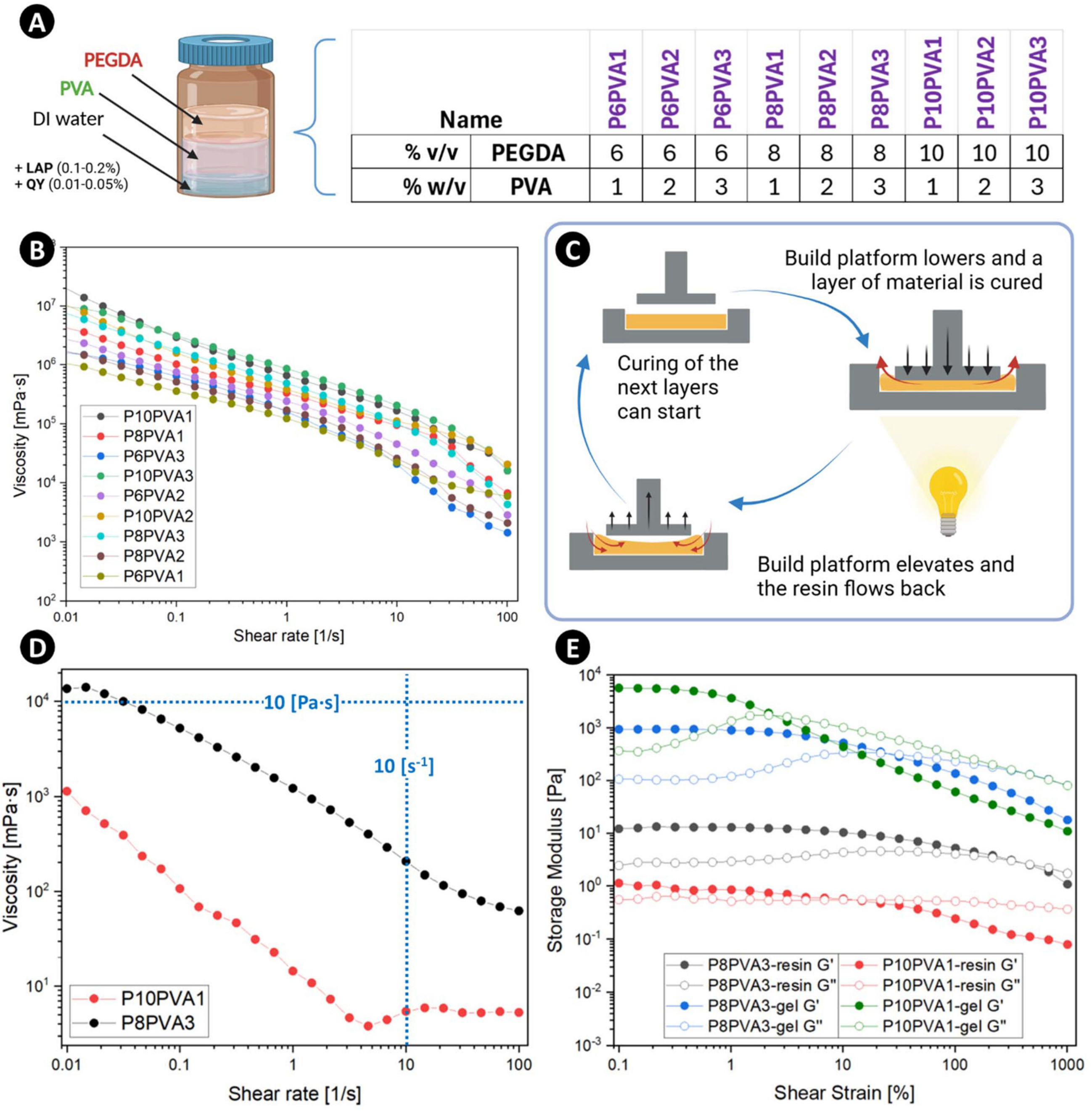

Name		P6PVA1	P6PVA2	P6PVA3	P8PVA1	P8PVA2	P8PVA3	P10PVA1	P10PVA2	P10PVA3
% v/v	PEGDA	6	6	6	8	8	8	10	10	10
% w/v	PVA	1	2	3	1	2	3	1	2	3

Fig. 1 (A) Illustration of the biomaterial resin formulations and the table specifying the amounts of PEGDA and PVA; LAP – lithium phenyl-2,4,6-trimethylbenzoylphosphinate, QY – quinoline yellow. (B) Viscosity plots for the various hydrogel formulations (representative plots, *n* = 3). (C) Schematic of the DLP-printing process, illustrating the material flowability and gap refiling during the curing of the preceding layer. (D) Viscosity plots for the selected resins (P8PVA3, P10PVA1) (representative plots, *n* = 3). (E) Amplitude sweep tests for the selected resins (P8PVA3, P10PVA1) and the corresponding hydrogels. *G′* stands for storage modulus and *G″* for loss modulus (representative plots, *n* = 3).

strain, indicating its greater structural stability under deformation. Additionally, the lower resin viscosity of P8PVA3 enhanced its flowability and suitability for DLP.

2.2 Fabrication of pre-designed models using DLP

The successful fabrication of pre-designed models using DLP requires adjustments of the input parameters, including the layer exposure time, LED light intensity, and curing layer height, as well as the concentrations of the photoabsorber and photoinitiator.[34] To identify the successful printing conditions for our biomaterial resin (P8PVA3), we varied the layer thickness (50, 100, 150, and 200 μm) and light intensity (5, 10, 15, 20, and 25 mW cm^{-2}), while keeping the exposure time at 8 s. The resin could be successfully cured on the build platform using a layer thickness of 100 µm, light intensity of 15 mW cm^{-2}, and a curing time of 8 s (Fig. 2A, see the ticks in the diagram).[35]

Quinoline yellow (QY) was utilized as a photoabsorber to prevent excessive crosslinking and optimize the print resolution.[5] However, the inclusion of QY at a concentration of 0.01% (w/v) slowed the polymerization, requiring an extended exposure time from 15 s to ~50 s for curing. To compensate for this, we increased the concentration of the photoinitiator (LAP) from 0.2% (w/v) to 0.4% (w/v), which restored the curing times to approximately 15–20 s. This observation aligns with previous reports suggesting that the QY concentration can also influence the photopolymerization kinetics.[20]

To assess the resolution limits of the DLP-printing process with our resin, we designed a comb-hole model to include both protrusions (positive features) and hollow cavities (negative features) with increasing dimensions (Fig. 2B). We succeeded in printing 41 µm holes, which were approximately 9 µm smaller than the designed size, demonstrating the precision of the system (Table 1). However, when fabricating 50 µm protrusions, they failed to detach from the platform, likely due to the soft nature of the material (Fig. 2B). We could successfully obtain positive features sized 108.4 ± 7.2 µm for the 100 µm designs. These dimensional differences may be attributed to a slight overcuring of the resin.

To show the versatility of the P8PVA3 resin, various models, including flower-shaped objects, vein-like structures, and crochet infills, were printed (Fig. 2C–E). Notably, despite the high-water content of the resin formulations (>85% v/v), the 3D-printed structures exhibited fidelity, with sharp and well-defined edges. However, when the object printing height exceeded 30–40 mm, the samples deformed slightly due to drying.[36] To address this limitation, environmental humidity control using an enclosed, humidified printing setup or reducing the overall printing duration may help reduce drying-induced deformation and enable the fabrication of objects taller than 30–40 mm.

2.3 Post-processing of the DLP-printed constructs

The acrylate groups of PEGDA undergo photopolymerization in the presence of the LAP and upon exposure to visible light

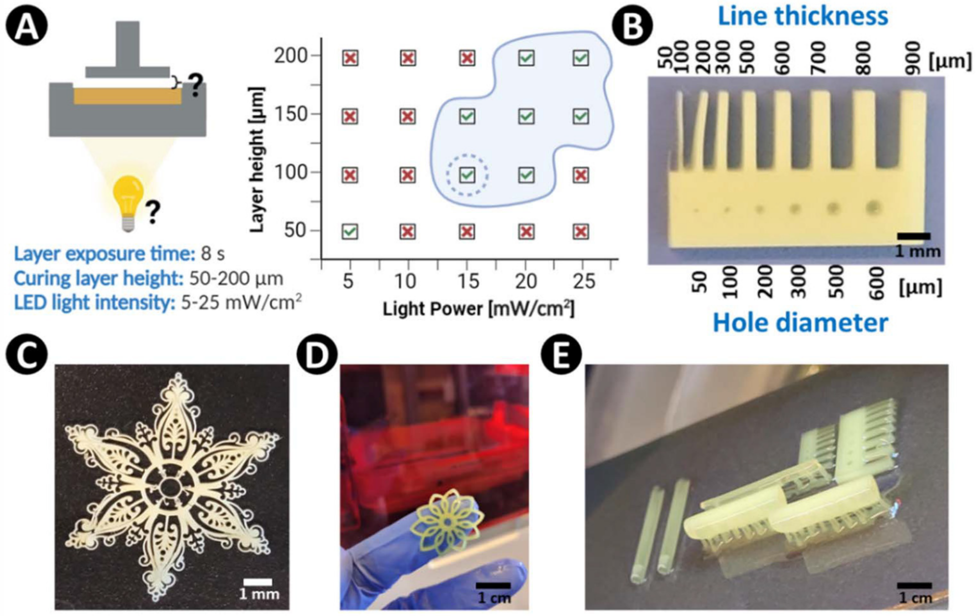

Fig. 2 (A) Tuning the DLP-printing process for the P8PVA3 biomaterial resin; the layer exposure time was kept constant (8 s), while the LED light intensity and curing layer height were varied; tests were performed in triplicate (n = 3) for each condition of the layer height and light power. (B) Comb-shaped template with holes to assess the resolution of the printing technology and synthesized resin materials (size increments of 50, 100, 200, 400 µm, *etc.*). (C) Snowflake with crochet-inspired infill. (D) A 100 µm thin flower-shaped object. (E) Various geometries fabricated in a single DLP process, arranging the parts for batch processing; note that some objects have support structures, which can be easily removed during post-processing.

Table 1 Resolutions of the 3D-printed positive and negative features; n = 3, mean ± SD

	Designed size	DLP-printed	%difference from the designed size
Smallest positive feature	100 µm	108.4 ± 7.2 µm	8.4
Smallest negative feature (hole)	50 µm	41.2 ± 3.8 µm	17.6

(>30 s, 405 nm) (Fig. 3A).[37] The FTIR spectrum of PEGDA displayed characteristic peaks at 2866 (C–H stretching), 1729 (C═O stretching), and 1094 cm^{-1} (C–O stretching).[38] FTIR analysis of the PEGDA-PVA hydrogel revealed a characteristic peak in the range of 3100–3550 cm^{-1} attributed to the hydroxyl groups of PVA,[39] confirming the successful incorporation of PVA into the PEGDA network (Fig. 3D). The broad peak ranging from 3100 to 3550 cm^{-1} in the FTIR spectra of PVA and PEGDA-PVA suggests the presence of hydrogen bonding between the hydroxyl groups of PVA.[39]

To induce secondary crosslinking and enhance the bioactivity, PEGDA-PVA hydrogels were treated with 5% wt/v borax (Fig. 3B) and 5% wt/v TA solutions (Fig. 3C). These treatments further interlocked the PVA chains present in the hydrogels by creating PVA-borax and PVA-TA complexes (Fig. 3B and C). The chemical interactions between the two components can alter the FTIR spectrum, often through the appearance of new peaks or shifts in characteristic peaks.[40] The characteristic peak ranging from 3100 to 3550 cm^{-1}, attributed to the hydroxyl groups of PVA in the FTIR spectrum of PEGDA-PVA, was flattened and shifted to a range of 3200 to 3550 cm^{-1} after

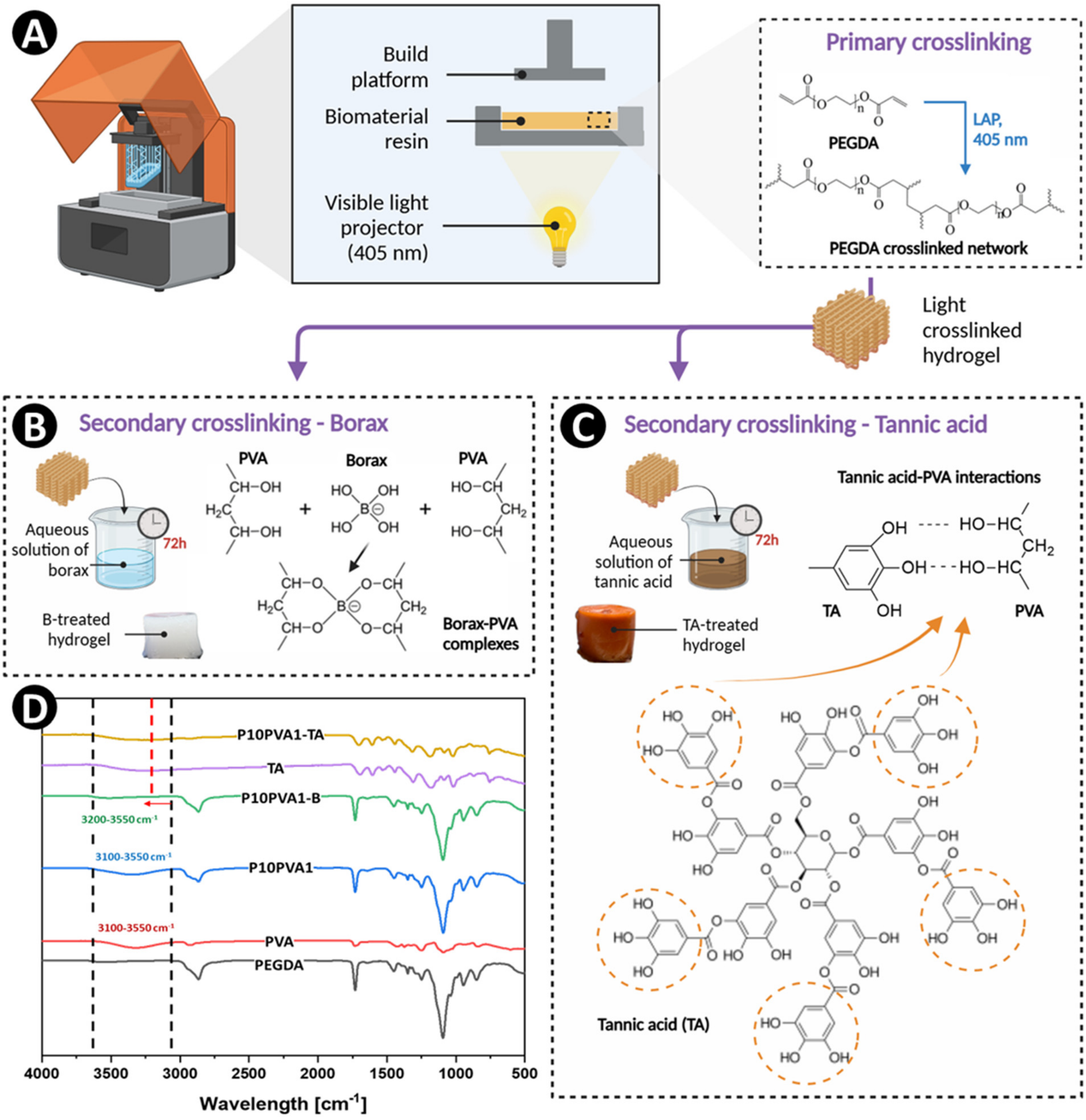

Fig. 3 (A) Schematics depicting the DLP fabrication process along with PEGDA crosslinking mechanism occurring and the interface of the build platform and biomaterial resin. (B) Schematic shows the hydrogel secondary crosslinking with borax. (C) Schematic shows the hydrogel secondary crosslinking with tannic acid (TA). (D) FTIR spectra of different hydrogel formulations.

treatment with borax, indicating the formation of borate-PVA complexes as previously reported.[40]

The broad peak at 3100 to 3550 cm^{-1} in the TA-treated hydrogel was similar to that of TA, suggesting potential surface coverage of the hydrogel by TA. Strong hydrogen bonding between TA and PVA was previously reported by Chen *et al.*, who observed a shift in the hydroxyl group peaks from 3268 cm^{-1} for TA and 3276 cm^{-1} for PVA to 3253 cm^{-1} in the FTIR spectrum of PVA treated with TA.[24] Fig. 3B and C show images of the untreated and TA-treated P10PVA1 hydrogels. The darker brown color of the treated hydrogel confirmed the presence of TA on its surface.

The interlocking of PVA with borax and TA *via* di-diol and hydrogen bonding, respectively, was expected to enhance the mechanical and rheological properties of the hydrogel. Therefore, the impacts of the TA and borax treatment on the mechanical and rheological properties of the PEGDA-PVA hydrogels were investigated (Fig. 4A–E).

Treatment with borax enhanced the compressive modulus and toughness of both the PEGDA-PVA hydrogels (P8PVA3 and P10PVA1) (Fig. 4B and C). After borax treatment, P8PVA3 exhibited an increase in compressive modulus from 9.2 ± 1.2 kPa to 14.4 ± 0.9 kPa, compared to a decrease to 7.6 ± 0.5 kPa for the TA-treated samples (Fig. 4B),[41] which could be attributed to its higher content of hydroxyl groups for crosslinking with borax.[42] Indeed, the borate–ester bonds between the hydroxyl groups of PVA act as physical crosslinking points within the matrix, thus increasing both the rigidity and strength.[18] Previous studies have reported an increase in the mechanical properties of PVA hydrogels with increasing borate crosslinking density, confirming the positive correlation between the borate–ester interactions and mechanical strength.[42]

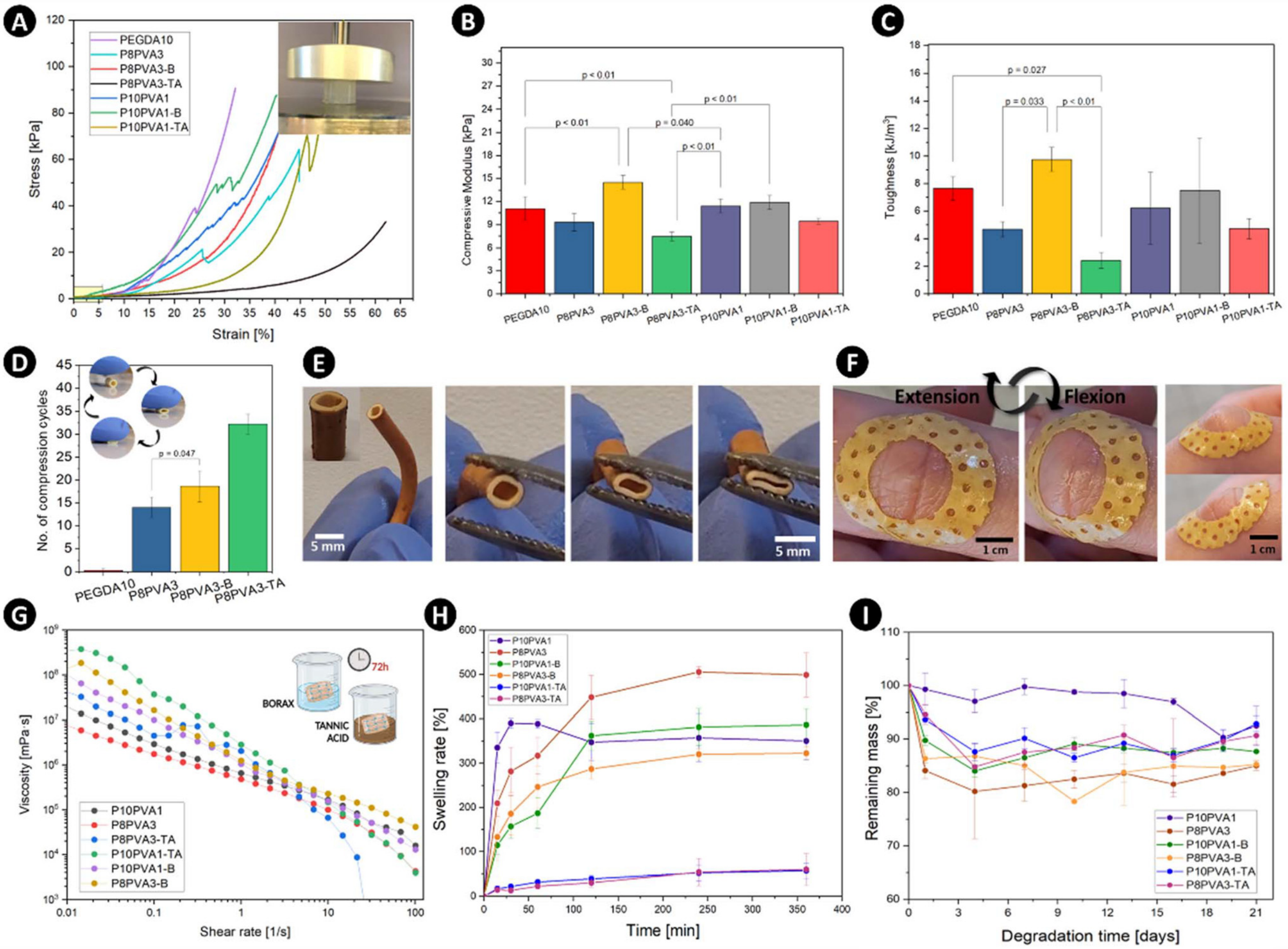

Fig. 4 (A) Stress–strain plot from the compression tests of various constructs, (representative plots based on $n \geq 3$). (B) Compressive moduli of the hydrogels ($n \geq 3$, mean ± SD). (C) Toughness of the hydrogel samples (≥3, mean ± SD). (D) Comparison of the number of compression cycles before the failure of tubular grafts made of P8PVA3 with borax or tannic acid secondary crosslinking ($n \geq 4$, mean ± SD). (E) Fabricated vein-like structure (2 mm in diameter and 40 mm long) subjected to compression–relaxation forces, demonstrating the high shape-fidelity and stability of the biofabricated structures with TA treatment. (F) Thin (2 layers) circle-shaped adhesive bandage, withstanding finger bending, top and side views. (G) Viscosity of the P8PVA3 and P10PVA1 hydrogels upon secondary crosslinking with borax (B) or tannic acid (TA) (representative plots, $n = 3$). (H) Swelling of the constructs with and without secondary crosslinking with borax and tannic acid, ($n = 3$, mean ± SD). (I) Degradation rate of the fabricated constructs ($n = 3$, mean ± SD).

In contrast to borax treatment, the TA-treated hydrogels exhibited a reduced compressive modulus and toughness compared to the untreated hydrogels, while increasing the strain (Fig. 4B and C). For example, the compressive modulus of P10PVA1 decreased from 11.4 ± 0.9 to 9.4 ± 0.4 kPa after treatment with TA. The reduction in the compressive modulus may be attributed to hydrogen bond formation between the TA molecules.[43] It has been previously reported that a high concentration of TA can lead to intermolecular hydrogen bonding between TA molecules, diminishing the tensile strength of PVA hydrogels.[43] At elevated TA concentrations, the penetration of TA into the hydrogel network may be hindered, limiting hydrogen bonding interactions with PVA and thus contributing to the observed reduction in mechanical properties.[43] Thus, the reduction in mechanical properties observed in the TA-treated hydrogels in our study may have resulted from the limited penetration of TA into the hydrogel network. This interpretation is supported by the similarity in the FTIR spectrum of the treated hydrogels to that of pure TA (Fig. 3D).

The PEGDA hydrogels could be made more flexible by incorporating PVA and by treatment with TA (Fig. 4D–F). Unlike the PEGDA-only designs, the PEGDA-PVA (P8PVA3)-printed tubes could be repeatedly compressed and still retain their shape. Cyclic compression tests showed that the P8PVA3-printed tubes after TA treatment (P8PVA3-TA) (Fig. 4D) had the highest durability, remaining intact after ∼32 cycles. Significantly lower numbers of cycles were achieved for P8PVA3-B and P8PVA3, namely only ∼19 and ∼14 cycles, while the PEGDA-only tubes failed immediately. Furthermore, the P8PVA3 tubes with TA treatment could be easily handled and bent without breaking (Fig. 4E). In our next design, we aimed to show the influence of TA treatment on the printed constructs' adhesiveness. Previous studies have shown that TA interacts with polymers by forming multiple hydrogen bonds, which enhances their adhesiveness to various substrates, including skin, wood, plastic, and glass.[44] To explore this, we fabricated a thin, bandage-inspired hydrogel sheet treated with TA (Fig. 4F). When applied to the skin, this hydrogel construct demonstrated adhesion, remaining intact through multiple cycles of finger extension and flexion without detaching.

Fig. 4G shows that TA treatment enhanced the viscosity of the P10PVA1 and P8PVA3 hydrogels by 13 and 6 times, respectively, which could be due to hydrogen bonding between the hydroxyl groups of TA and the alcohol and ether groups in PVA and PEGDA.[25,45] Borax treatment increased the viscosity of the P10PVA1-B and P8PVA3-B hydrogels by 5 and 14 times, respectively, due to the formation of borax-PVA complexes, which created a tightly bonded network.[18] However, at shear rates above 1 s^{-1}, the influence of the TA and borax treatment was not evident, likely because higher shear rates disrupt the hydrogel network, making it deform and flow more easily.[46]

2.4 Physical properties of the post-printing treated hydrogels

The swelling capacity is a crucial property of a hydrogel, showing its ability to absorb fluid and create a swelled 3D matrix supportive for cell activities.[47] The highest swelling ratio of around 500% was achieved for the P8PVA3 hydrogel after 4 h, while the P10PVA1 hydrogel with a lower content of PVA swelled up to 350%, but after only 0.5 h (Fig. 4H). This increased swelling capacity of the P8PVA3 hydrogel may be linked to the presence of more –OH groups in the P8PVA3 hydrogel, which could form more hydrogen bonds with water. Borax treatment decreased the swelling ratio of the P8PVA3 hydrogel to approximately 320%, while the borax-treated P10PVA1 hydrogel did not show a significant difference in swelling ratio compared to the P10PVA1 hydrogel. This may be justified by the presence of more –OH groups in the P8PVA3 hydrogel, which were responsible for creating complexes with borax, thereby tightening the hydrogel network. The hydrogels treated with TA showed the creation of secondary crosslinks between TA and the PVA and PEGDA through multiple hydrogen bonds, which decreased their capacity to absorb water, similar to a previous study that showed a lower swelling of the PEGDA hydrogel after treatment with TA.[24] The equilibrium swelling was around 50% for the TA-treated hydrogels, which was lower than for the non-treated samples, as was similarly reported previously.[48] All the hydrogels exhibited good stability, with a low mass loss observed during three weeks of incubation in PBS at 37 °C (Fig. 4I). Increasing the concentration of PVA from 1% to 3% accelerated the degradation of both untreated and borax-treated hydrogels. This effect is attributed to the enhanced hydrophilicity imparted by the hydroxyl groups of PVA. TA treatment resulted in improved stability of the hydrogels *via* the formation of strong hydrogen bonds between its hydroxyl groups and the hydroxyl groups of PVA, as similarly reported for TA-treated chitosan hydrogel.[48]

The morphology and porosity of the hydrogels, which play crucial roles in cell adhesion, growth, and differentiation,[49] were examined using scanning electron microscopy (SEM). The hydrogels displayed porous structures (Fig. 5A). Although no surface differences were observed between the hydrogels upon treatment with borax or TA, the internal structures showed a decreased pore size. The observed reduced pore size and porosity in the TA- and borax-treated hydrogels could be attributed to the formation of denser structures due to the intermolecular interaction from the hydrogen bonds of TA with PVA and PEGDA as well as the borate–ester bonds between borax and PVA.

Additionally, porosity and pore-size measurements were carried out on freeze-dried hydrogels using micro-CT (micro-computed tomography) analysis. This technique was used because SEM could not provide clear information about the internal porous structure of the tested materials and whether it was homogeneous in the entire sample volume.[50] Micro-CT has previously allowed visualizing, analyzing, and characterizing the 3D structure of hydrogels. For instance, Carvalho *et al.*[51] used this technique to visualize the porous structure of chitosan–gelatin hydrogel hybrids. Also, Douglas *et al.*[52] successfully used micro-CT to check the homogeneity of chit-

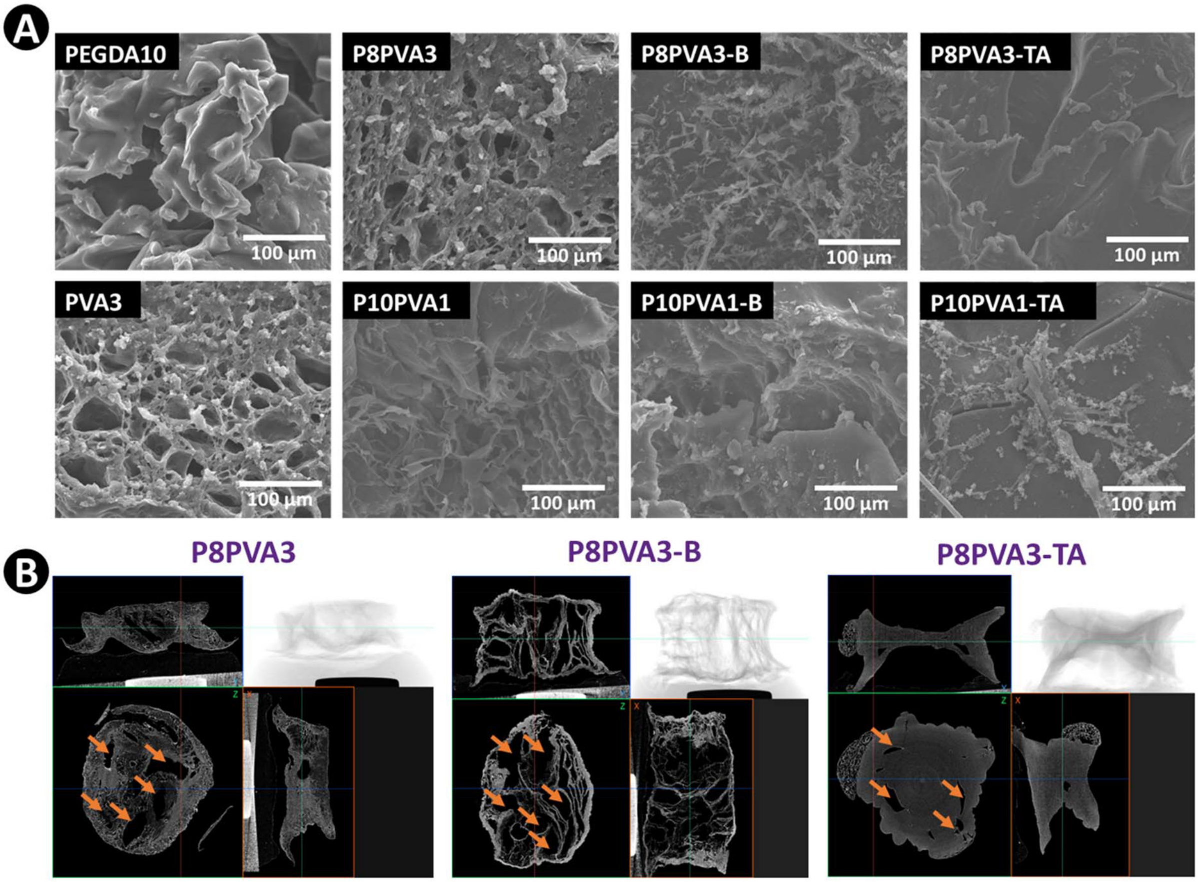

Fig. 5 (A) SEM cross-sectional images of different hydrogels. (B) Micro-CT scanning images of different lyophilized hydrogels; orange arrows indicate the presence of pores in the horizontal cross-section.

osan hydrogels. The micro-CT 3D visualization images of the hydrogels are shown in Fig. 5B. It can be clearly observed that the hydrogels presented porous structures. P8PVA3-B displayed smaller pores compared to P8PVA3. This observation may be attributed to the formation of strong intermolecular borate–ester bonds between the borax and PVA, leading to a denser and more compact hydrogel structure. The lower porosity exhibited by the P8PVA3-TA hydrogel was likely because the incorporation of TA into the hydrogel network facilitated the formation of numerous hydrogen bonds between the TA, PVA, and PEGDA, resulting in increased structural densification and a subsequent reduction in the average pore size. However, we acknowledge that the freeze-drying process used for sample preparation can introduce artifacts, such as shrinkage, collapse of the pore structure, or alterations in the pore-size distribution due to the sublimation of ice crystals. These changes may not fully represent the native hydrated morphology. Therefore, while micro-CT provides valuable insights into the internal architecture, the results should be interpreted with caution, and future work could benefit from complementary imaging methods that preserve the hydrated state of the materials.

2.5 Hydrogels properties upon tannic acid (TA) treatment

The release of bioactive molecules from hydrogels is crucial for tissue healing by promoting cell proliferation, and differentiation or by preventing inflammation.[53] The structure of the hydrogel matrix and the available active sites influence the adsorption of the TA in the hydrogel and its release profile.[54] The loading efficiency indicates the amount of TA loaded in the hydrogel with respect to the amount of TA utilized for the functionalization of the hydrogels.[54] Here, TA could be loaded with an efficiency of 39.00 ± 2.97% in the P8PVA3 hydrogel and 34.02 ± 3.33% in the P10PVA1 hydrogel.

The *in vitro* release of TA from the P8PVA3-TA and P10PVA1-TA hydrogels was investigated using UV spectrophotometry at 278 nm.[55] It was found that the TA was gradually released to the medium and the percentage release reached 64.36 ± 0.47% from the P8PVA3-TA hydrogel and 59.55 ± 19.05% from the P10PVA1-TA hydrogel in 10 days (Fig. 6A). The sustained release of TA from the hydrogels could be attributed to the successful functionalization of the hydrogels with TA through the formation of hydrogen bonds between the hydroxyl functional groups of TA with the functional groups of PVA and PEGDA.[25,45] No significant difference was observed in the TA release profile between these two hydrogels, mainly because of their similar swelling patterns (Fig. 4H). The presence of functional hydroxyl and carbonyl groups in the PVA and PEGDA structures could likely contribute to the release of TA due to their role in aiding the swelling of the hydrogels and then facilitating the release process.[54] The release of a low concentration of TA from the adhesive PVA-TA composite was reported by Lee *et al.*, which continued for 6 days.[45] To understand the release mechanism of TA from the hydrogels, we performed release kinetic modeling as this can provide valuable information about the mechanism controlling the TA release and its release rate from the hydrogel matrix.[56] The cumulative release data (Fig. 6A) obtained for the P8PVA3-TA and P10PVA1-TA hydrogels were fitted into the three kinetic models, namely the zero-order (Fig. 6B), Korsmeyer–Peppas (Fig. 6C) and Higuchi (Fig. 6D) models. It was found that the Higuchi kinetic model could best explain the release mechanism of TA from both the P8PVA3-TA and P10PVA1-TA hydrogels as the plot showed the highest coefficient of determination (R^2 > 0.97), suggesting that the release process of TA could be controlled by Fickian diffusion.[57] TA release also showed good correlation with the Korsmeyer–Peppas model, with good linearity (R^2 > 0.96). The Korsmeyer–Peppas model, as a semi-empirical model, was applied to better describe the release mechanism. In this model, depending on the release exponent (n) value, the release mechanism is controlled by the Fickian diffusive process ($n \approx 0.45$), representing anomalous transport, which is a combination of diffusion and swelling

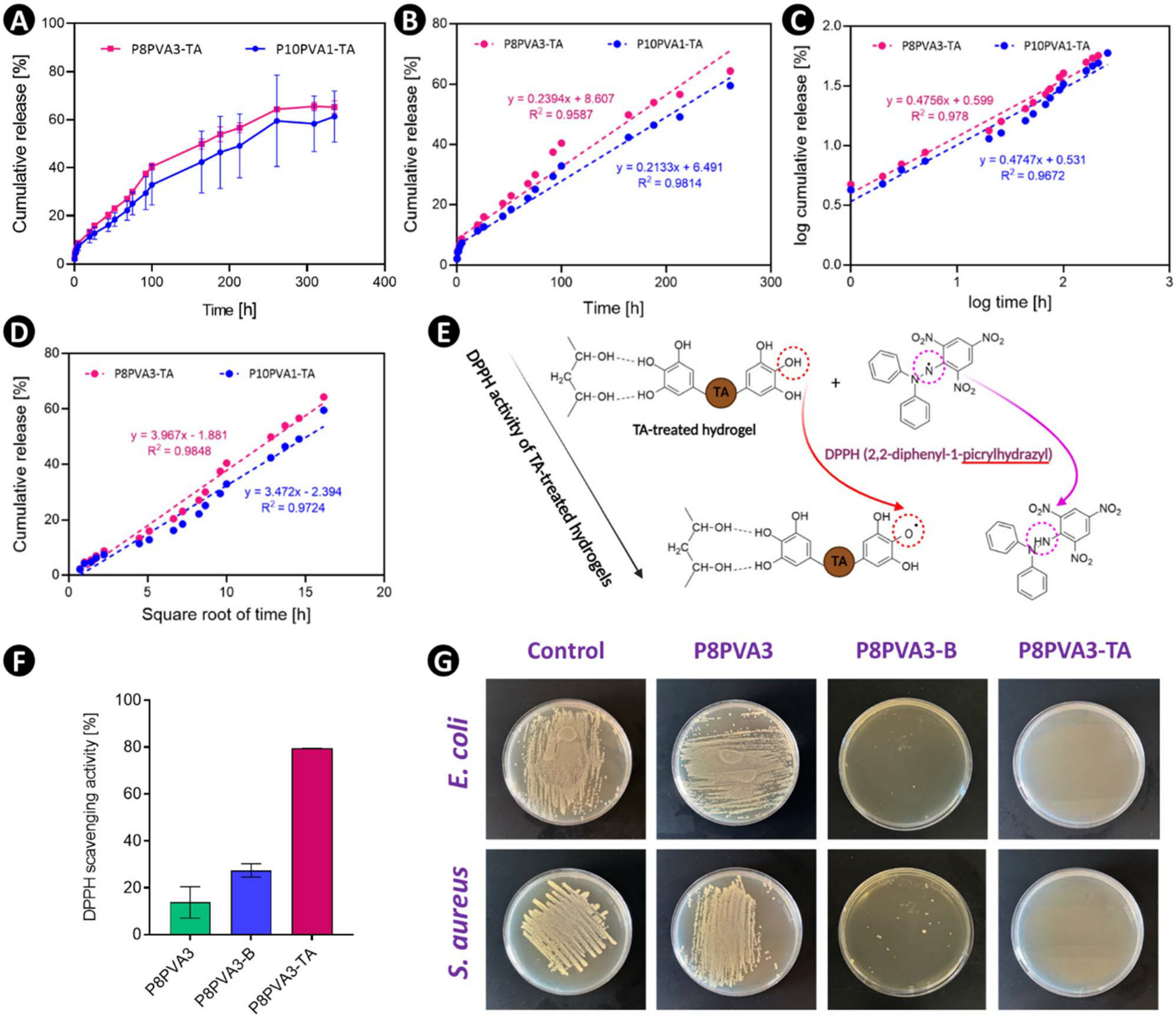

Fig. 6 (A) Tannic acid release from P10PVA1-TA and P8PVA3-TA hydrogels, (n = 2, mean ± SD); (B–D) kinetic tannic acid release models: (B) zero-order; (C) Korsmeyer–Peppas and (D) Higuchi models. (E) Schematic illustrating the DPPH radical scavenging activity of tannic acid. (F) DPPH radical-scavenging activities of the P8PVA3, P8PVA3-TA, and P8PVA3-B hydrogels (n = 2, mean ± SD). (H) Inoculated agar plates with bacteria exposed to the hydrogels after 1 day of incubation.

($0.45 < n < 0.89$), and swelling ($n > 0.89$).[58] The n value in our study was measured as 0.47 for the P8PVA3-TA and P10PVA1-TA hydrogels, indicating that an anomalous diffusion mechanism, a combination of diffusion and polymer swelling or erosion, mainly controlled TA release from the polymeric matrix, with TA released with a kinetic constant K of 3.98 mg mL^{-1} $h^{-0.47}$ for P8PVA3-TA hydrogel and 3.40 mg mL^{-1} $h^{-0.47}$ for P10PVA1-TA. Upputuri *et al.* reported that the release of green tea polyphenol encapsulated in casein nanoparticles was controlled by an anomalous diffusion mechanism by achieving n values ranging from 0.54 to 0.71 for different loading concentrations, pH, and temperature.[59] Another study by Ciolacu *et al.* showed that the composition of cellulose-lignin hydrogels controlled the release of a polyphenolic extract of grape seed from the hydrogels, and the release behavior was shown to be controlled by an anomalous diffusion mechanism in several hydrogel compositions.[60] Biomaterials with antioxidant activity have shown promising results in scavenging free radicals and reducing the oxidative stress caused by ROS. Tannic acid as a bioactive molecule possesses antioxidant activity due to its hydroxyl groups in the catechol and galloyl groups.[23] For instance, the DPPH radical-scavenging activity was 96% for a TA-treated phenolated chitosan-alginate hydrogel and 84% for a silk-wool hydrogel functionalized with TA.[48,61] We investigated the antioxidant activity of P8PVA3 hydrogels treated with TA and borax, by performing a DPPH radical-scavenging activity assay (Fig. 6F). The results reveal that P8PVA3 did not have antioxidant activity, while P8PVA3-B hydrogels had low antioxidant activity. However, the TA-treated hydrogel demonstrated a 79.38 ± 0.17% DPPH radical-scavenging activity. This result aligns with the findings of Hong and Azadikhah *et al.*, who found that PVA and PVA-chitosan hydrogels could scavenge 92% and 90% of DPPH free radicals when treated with TA.[62,63] We expect that the released TA, having a high amount of OH functional groups, could scavenge free radicals by donating hydrogen atoms to the DPPH free radicals and converting them to stable reduced DPPH molecules (DPPH-H) without oxidative activity (Fig. 6E).[64]

We carried out antibacterial tests to evaluate the bacterial response to TA-treated, borax-treated, and non-treated P8PVA3 hydrogels (Fig. 6G). The P8PVA3 hydrogel showed no visible antibacterial activity, with *E. coli* and *S. aureus* growth comparable to the control. The P8PVA3-B hydrogel exhibited antibacterial effects, likley due to the antimicrobial properties of borax.[65] Almost no *E. coli* or *S. aureus* could be seen after coculture with P8PVA3-TA, which may be attributed to the antibacterial activity of TA.[66] In a previous study, a crosslinked scaffold based on glycol chitosan (GCS) with PEGDA displayed antimicrobial activity against *S. aureus*, with an inhibition rate of 80%.[67] While in another study, a double-network (DN) hydrogel dressing based on PEGDA and catechol-modified hyaluronic acid (C-HA) showed slight antibacterial activity against both *S. aureus* and *E. coli*, with antibacterial rates consistently less than 25%.[68] The results demonstrate that the TA-treated and borax-treated hydrogels possessed superior antimicrobial activity.

2.6 Cytocompatibility assessment of the treated hydrogels

To assess the cytocompatibility of the PEGDA-PVA hydrogels, we performed *in vitro* cultures of 3T3-L1 fibroblast cells with the hydrogels and assessed their viability using the MTS assay after 24, 48 and 120 h (Fig. 7A–C). We found that the cell viability remained above 70% at all the tested time points (24, 48, and 120 h), indicating the biocompatibility of the hydrogels in accordance with ISO 10993-5:2009.[69] Furthermore, no significant differences in cell viability were observed among the different hydrogel formulations (Fig. 7A–C), suggesting that the presence of B and TA in the hydrogels did not negatively affect the cell viability at the tested conditions. However, the cell viability of the hydrogels was lower compared to the control (cell culture plates) at all the time points (24, 48, and 120 h). This reduction may be attributed to a decrease in the number of cell adhesion sites on the hydrogels relative to the standard cell culture plates or gelatin-coated plates surfaces, as previously reported.[70] Additionally, the lower viability might also have resulted from the leaching of unreacted components or pH changes induced by the presence of the polymers. A color shift in the culture medium to yellow during the assay suggested potential acidification, although no direct pH measurements were performed to confirm this. Therefore, further studies are needed to investigate the underlying causes of the reduced cell viability of the hydrogels compared to the control, which represents a limitation of the current study.

Performing live/dead staining (Fig. 7D), no excessive cell death was noted for any of the samples and the cultured 3T3-L1 fibroblast cells exhibited good, elongated morphologies with clearly manifested F-actin fibers (Fig. 7E). These results confirmed the hypothesis that B and TA treatment can be used as a strategy to enhance materials' mechanical properties without compromising cell viability. It was reported that functional coatings could be applied to the polymer surface to facilitate cell attachment and the formation of a uniform layer of endothelium.[71]

To further evaluate the samples' biocompatibility, *in vivo* tests were performed on a larval model (*Galleria mellonella*). The *G. mellonella* model has several advantages over the mammalian model, *e.g.*, it does not require ethical approval, larval maintenance is inexpensive, manipulation is easy, and its allow rapid experimental execution.[72] We first investigated the ingestion of the samples by *G. mellonella*. The ingestion (Fig. 8A and C) was at a similar level and did not result in larval mortality. The ingestion levels for P8PVA3 and P8PVA3-TA were comparable and did not result in larval mortality, whereas P8PVA3-B led to irregularities in the structure of the epithelial cells (Fig. 8Diii) and showed slight adverse effects on larval health.

Additionally, in the test assessing larval mortality (Fig. 8B) when wrapped with the samples (Fig. 8E), the highest mortality rate of 1 out of 3 larvae was observed in the larvae wrapped with P8PVA3-B, compared to no death incidents for the larvae wrapped with P8PVA3. In summary, the use of P8PVA3-B correlated with a certain level of undesired effects.

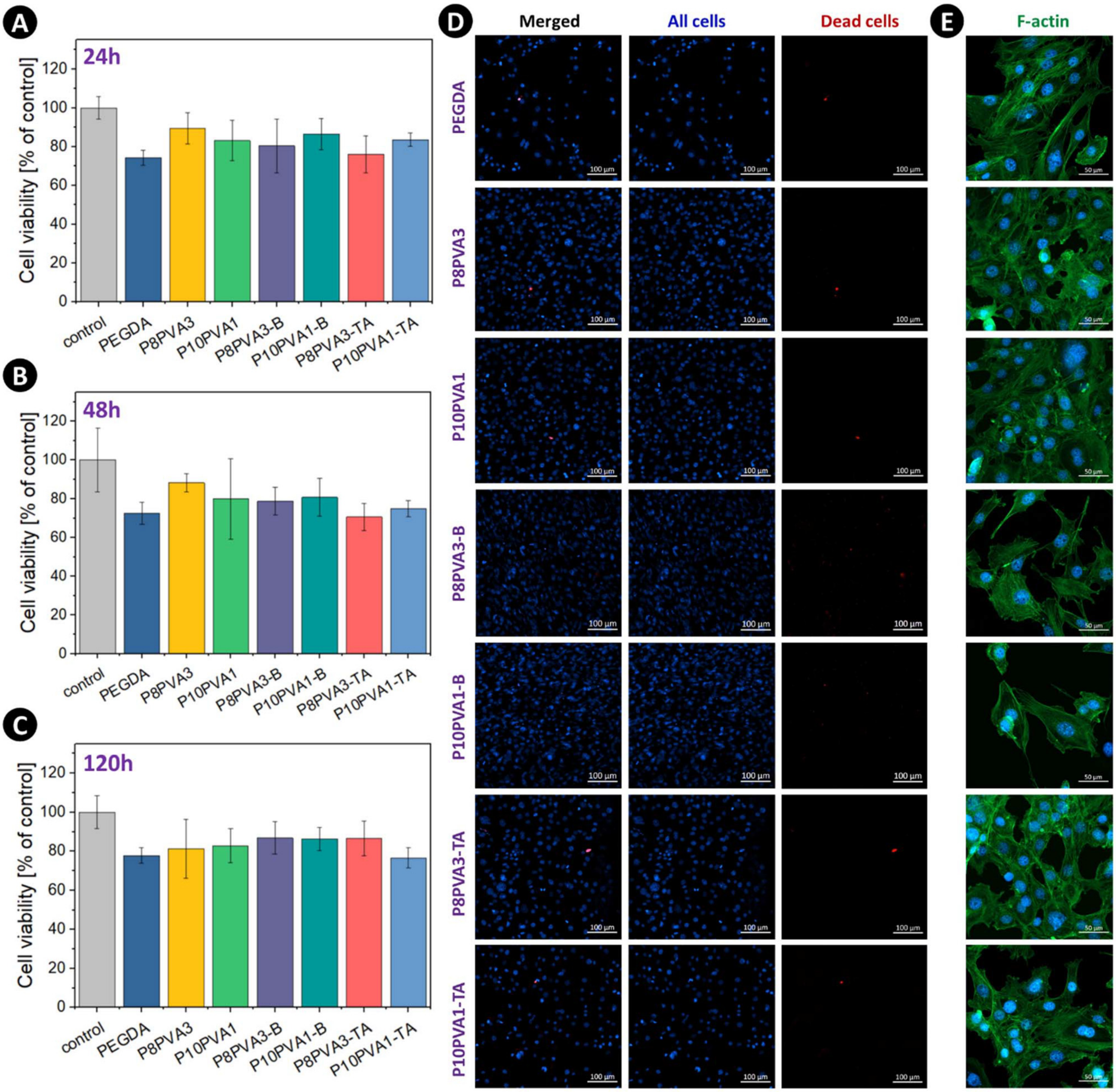

Fig. 7 Cell viability results after (A) 24 h, (B) 48 h, and (C) 120 h for cells cultured with PEGDA, P8PVA3, P10PVA1 and borax- or tannic acid-treated samples (cells cultured on a culture plate were used as an experiment control, showing 100% viability), (n = 4, mean ± SD, populations were significantly different from the control at p = 0.05). (D) Live/dead staining of 3T3-L1 cells cultured with different hydrogels. (E) Confocal images showing the cell cytoskeleton stained in green (Alexa Fluor 488-Phalloidin) and nuclei in blue (Hoechst).

Therefore, this sample requires further scrutiny, particularly in *in vivo* experiments using mammalian models, to evaluate the potential adverse effects.

3. Conclusions

In this project, we designed a two-component biomaterial resin composed of PEGDA and PVA. The light-triggered polymerization of PEGDA and the creation of an interpenetrating network composite with PVA resulted in a robust and flexible PEGDA-PVA hydrogel. Secondary crosslinking achieved by borax or TA treatment reduced the brittleness of the PEGDA-only hydrogel, while gradual TA release endowed the hydrogel with antimicrobial and antioxidant activities. DLP-printing technology allowed the fabrication of complex architectures, including hollow features with sharp edges, which are otherwise difficult to achieve with conventional extrusion-based printing processes. The PEGDA-PVA hydrogel, enhanced by borax and TA post-treatments, demonstrated improved

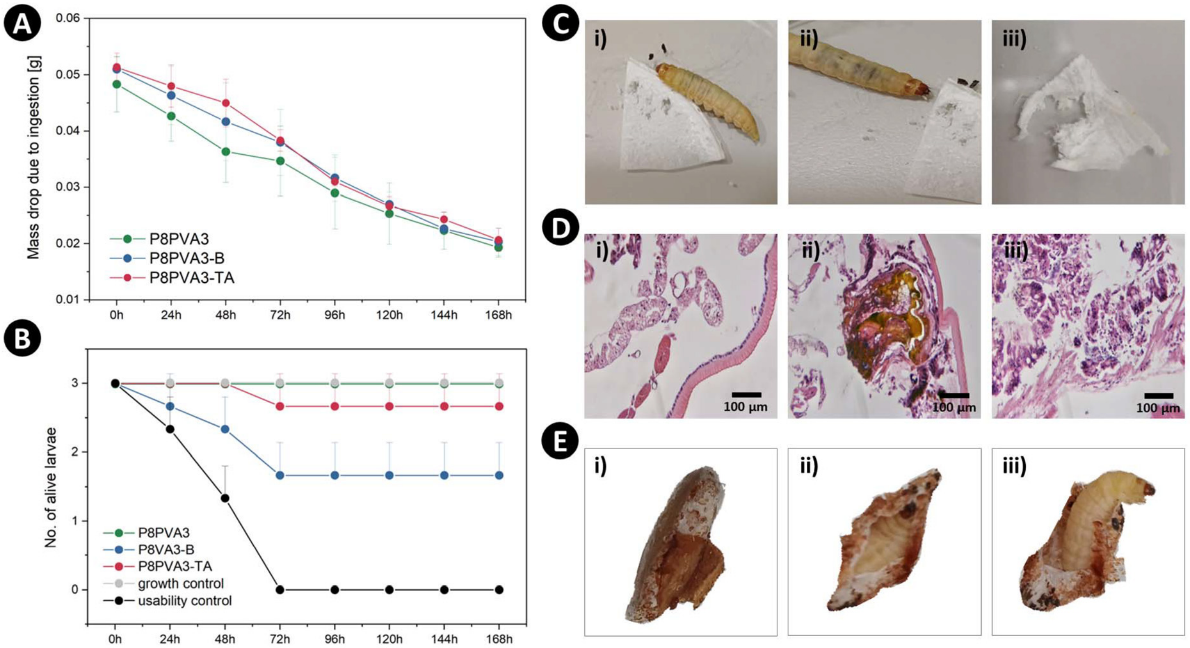

Fig. 8 (A) Reduction in the mass of samples being digested by larvae after 168 h of the experiment (n = 3, mean ± SD). (B) Mortality rate of the larvae after exposure to the samples (n = 9, mean ± SD). (C) i–ii – ingestion of the P8PVA3-B sample by the larvae; iii – P8PVA3-B sample after 168 h; (D) i – a distinct epithelium with an organized structure, suggesting that the tissue was in a physiological state, without visible signs of pathology, such as damage, inflammatory infiltrates, or cell degeneration (P8PVA3); ii – gut content (P8PVA3-TA); surrounding tissue appeared structurally intact and normal, suggesting no visible pathology. iii – irregularities in the structure of epithelial cells, indicating damage or a response to a stress factor (P8PVA3-B); (E) i–iii – larvae wrapped in the samples.

mechanical properties, antioxidant activity, and precision in DLP fabrication. However, acquiring a hydrogel with hierarchical porosity and controlling the lyophilization conditions, which could influence the microstructure and morphological properties of the hydrogels, remain challenges that need further exploration in future works. In addition, our future works will explore the optimum concentration of TA and B for the post-treatment of the DLP-printed PEGDA-PVA hydrogel.

4. Experimental section

4.1 Materials

Poly(vinyl alcohol) with a molecular weight of 72 000 g mol^{-1}, and ethanol were purchased from Chem-Lab (Zedelgem, Belgium). Sodium tetraborate decahydrate 99.5% ACS (Borax) reagent was purchased from Thermo Fisher Scientific (MA, USA). Tannic acid (95%), with a molecular weight of 1701.23 g mol^{-1}, was purchased from Acros Organics (under Thermo Fisher Scientific, MA, USA). poly(ethylene glycol) diacrylate (PEGDA) with a molecular weight of 700 g mol^{-1}, 2,2-diphenyl-1-picrylhydrazyl (DPPH), lithium phenyl-2,4,6-trimethylbenzoylphosphinate (LAP) with a purity ≥ 95%, and quinoline yellow as well as the inhibitor remover were provided by Sigma-Aldrich (St Louis, MO, USA). Phosphate buffer saline (PBS) was purchased from Invitrogen (St Louis, MO, USA).

4.2 Resin formulation and hydrogel preparation

The resin was prepared by mixing PEGDA and PVA solutions with a photoinitiator (LAP) and photoabsorber (QY). Before that, stock solutions of PVA (6% w/v), PEGDA (20% v/v), and borax (5% w/v) and TA (5% w/v) were prepared. PVA was dissolved in deionized water and heated and the inhibitor was removed from PEGDA using a filtration column and supplier-recommended inhibitor removers.[73] Next, a photoinitiator, LAP, was added to each formulation for photocrosslinking (0.2% w/v).

For treatment of the hydrogels, two formulations P10PVA1 and P8PVA3 were treated with TA and borax by immersing in TA and borax solutions for 72 h at room temperature in the dark for the TA-treated samples. Finally, they were washed with distilled water to remove un-bonded TA and borax from the hydrogels. For the cytotoxicity experiments, the as-prepared resins were filtered through a 0.22 µm membrane for sterilization.

4.3 Characterization

Fourier-transform infrared spectroscopy (FTIR). FTIR was used to determine the chemical structure of the hydrogels as well as their pure components. The resolution was 4 cm^{-1}, recorded within a range of 400–4000 cm^{-1} using a Bruker Alpha II instrument.[74]

Rheological properties. The rheological properties of the biomaterial resins and hydrogels, with and without borax and

TA treatment, were investigated using a rheometer (Anton Paar, MCR 302). The plate–plate measuring system was used at a temperature of 25 °C, with a 25 mm diameter probe, and the gap between the two plates was 1 mm. To test the rheological parameters of the composite resins, the gap was set to 0.3 mm. The sample was placed on the rheometer plate, and the excess was trimmed before the test. The viscosity of each sample was then recorded.[75]

Printability of the hydrogels. The hydrogels were 3D printed utilizing a DLP printer (ASIGA MAX 27X), with a 405 nm light source. Quinoline yellow, a water-soluble food dye, was used as a photoabsorber to ensure high-resolution printing.

To test the printability, the prepared PEGDA-PVA resin was transferred into a vat. The pre-designed models were converted into stereolithography (STL) files and sliced in the *Z* direction, considering the build layer thickness. The following slices were projected for every layer to create the pre-designed 3D object. The resin material was exposed to light irradiation (405 nm, 5–25 mW cm^{-2}) to cure the subsequent layers. Once printing was completed, the 3D hydrogel was removed from the build platform and washed with distilled water to remove any non-cured polymer.[35]

Compression tests. Compression tests (Shimadzu AGS-X, load cell of 20N) were carried out to verify changes in the mechanical performances of the PEGDA-PVA and pure PEGDA hydrogel and to determine the impact of the two TA and borax treatment strategies. Each hydrogel was placed between the machine's plates to undergo a single compression test at a crosshead speed of 1 mm min^{-1}. The hydrogels' compressive modulus was determined based on the slope of the linear region in the 0%–5% strain range of the stress–strain curves.[76] The toughness was determined by integrating the stress–strain curve, and was expressed as the mechanical deformation energy per unit volume before fracture.[77]

Antioxidant activity. The TA-treated hydrogels' antioxidant activity (% *A*) was identified according to the DPPH free radical-scavenging activity method described in the literature.[48] Hydrogels were immersed in 1 mL of DPPH solution (0.4 mM in ethanol 100%) and incubated at 37 °C in the dark for 30 min. After 30 min, the UV absorbance of the samples was measured at a wavelength of 517 nm using a microplate reader spectroscope (BioTek Instruments Epoch, USA). The % *A* of the hydrogels was then calculated according to the following equation (eqn (1)):

$$\% \ A = \frac{\mathrm{Ab}_{\mathrm{control}} - \mathrm{Ab}_{\mathrm{sample}}}{\mathrm{Ab}_{\mathrm{control}}} \times 100, \quad (1)$$

where $\mathrm{Ab}_{\mathrm{control}}$ and $\mathrm{Ab}_{\mathrm{sample}}$ represent the absorbance of the control (DPPH solution) and the sample (DPPH solution with hydrogel), respectively.

Swelling and degradation. The swelling properties of the hydrogels with and without borax and TA treatment were investigated (n = 3).[78] The hydrogels were first freeze-dried, weighed, and then immersed in 3 mL of PBS (1×) in a sealed 24-well plate, and kept at 37 °C. After 15 min, 30 min, 1 h, 2 h, 4 h, and 6 h of incubation in PBS, the samples were removed and excess PBS was drained off with a paper towel, and then the sample mass was recorded. The swelling ratio was calculated according to eqn (2).

$$\mathrm{SR}\,(\%) = \frac{(m_{\mathrm{wet}} - m_{\mathrm{dry}})}{m_{\mathrm{dry}}} \times 100 \quad (2)$$

To investigate the degradation properties, the hydrogels with and without borax and TA treatment were first freeze-dried, weighed, and immersed in about 2–3 mL of PBS in a sealed 24-well plate, and kept at 37 °C. After various days, the samples were removed from the PBS and freeze-dried again. The remaining mass was calculated according to eqn (3).

$$\mathrm{RM}\,(\%) = \frac{m_{\mathrm{dayn}}}{m_{\mathrm{day0}}} \times 100 \quad (3)$$

***In vitro* release of tannic acid from the hydrogels.** The cumulative release of TA from the TA-treated hydrogels was determined by UV–Vis spectroscopy (Lambda 25 UV/VIS spectrometer) using a previously described method.[79] Briefly, the hydrogels were incubated in 15 mL PBS at 37 °C in the dark. Then, 1 mL of release media was withdrawn periodically for analysis with the UV spectrophotometer. The removed media was replaced with fresh media to keep the volume constant. The cumulative release of TA from the hydrogels was then quantified by measuring the UV–Vis absorbance of the TA in the release media according to the TA calibration curve obtained at a wavelength of 278 nm. The calibration curve was generated using TA standard solution ranging from 0.005 to 0.06 mg mL^{-1} with an R^2 value of 0.9953.

Kinetic modeling of tannic acid release. The kinetics of TA release from the hydrogels was investigated by applying three kinetic release models, namely the zero-order, Korsmeyer–Peppas, and Higuchi models, as described by the following equations (eqn (4)–(6)).[54] The models were applied to the mean values from the cumulative release data (Fig. 6A):

$$F = K_0 t \quad (4)$$

$$\frac{M_t}{M_\mathrm{e}} = K_{\mathrm{kp}} t^n \quad (5)$$

$$F = K_\mathrm{h} t^{1/2} \quad (6)$$

where F and M_t/M_e are the cumulative release of TA from the hydrogels at time t; and K_0, K_{kp}, and K_h represent the rate constants of the zero-order, Korsmeyer–Peppas, and Higuchi kinetic models, respectively.[54] To understand the mechanism of TA release, the exponent n value was calculated from the Korsmeyer–Peppas equation (eqn (5)) by plotting the first 60% of the cumulative release data.[57] The coefficient of determination (R^2), calculated by fitting the kinetic data into the simple linear regression model, was used to determine the most appropriate model for describing the release mechanism of TA from the hydrogel.

Biocompatibility and cell staining. The 3T3-L1 fibroblast cell line was used to investigate the properties of the PEGDA-PVA hydrogel material *in vitro*. The 3T3-L1 fibroblasts cells were maintained with Dulbecco's minimal essential medium (high glucose), supplemented with 10% FCS, 100 μg mL^{-1} penicillin, 100 U mL^{-1} streptomycin (Thermo Fisher Scientific), in a humidified CO_2 cell incubator (37 °C, 5% CO_2).[80]

To evaluate the hydrogels' biocompatibility and ability to serve as a support for cell growth and proliferation, the cells were cultured with the hydrogels for 24, 48, and 120 h. Cell viability was assessed using the MTS assay (CellTiter 96® Aqueous One Solution Cell Proliferation Assay, Promega, Madison, WI, USA). First, samples were washed with fresh cell medium, then, 100 μL of cell medium with 15 μL of MTS reagent was added to each well containing the sample. Control wells containing cells grown in the absence of hydrogels were used to normalize the cell viability to 100%. Samples were incubated at 37 °C for 3 h and protected from light.[81] Following incubation, the supernatant was recovered and transferred into a clean 96-well plate. The samples' absorbance was read at 492 nm using a microplate reader (Epoch, BioTek®, USA). The cell viability was calculated at various times to compare the absorbance values of the control wells containing cells grown in the absence of the hydrogel[19] (eqn (7)).

$$\text{Viability} = \frac{\text{Absorbance of sample}}{\text{Absorbance of control}} \times 100 \tag{7}$$

The distribution of live/dead cells cultured within the hydrogel specimens after 48 h was evaluated by incubating the cells at 37 °C for 45 min with 10 μg mL^{-1} Hoechst and 10 μM ethidium homodimer diluted in DPBS. Cytoskeleton staining (F-actin) was performed with 10 μg mL^{-1} Hoechst and 2 μM Alexa Fluor 488 – Phalloidin in DPBS, with 1% BSA.

Briefly, after washing the samples with DPBS and cell fixation for 20 min at 4 °C with 4% paraformaldehyde (PAF), the live and dead cells (blue- and red-colored cells, respectively) were observed through a fluorescent microscope (ZOE, Bio-Rad, Hercules, CA, USA). To evaluate the cellular morphology, the cells were fixed with 4% PAF for 30 min, followed by staining with 10 μg mL^{-1} Hoechst and 2 μM Alexa Fluor 488 – Phalloidin ((ab176753) – Abcam, Cambridge, UK) in DPBS, and 1% BSA at room temperature for 90 min. The samples were observed under a ZEISS LSM900 confocal, inverted microscope (Airscan mode, 10×, 20× objectives). Micrographs were randomly taken during the observation.[46]

Antibacterial activity. The antibacterial activities of the P8PVA3 hydrogel and B- and TA-treated hydrogels were assessed against Gram-negative *Escherichia coli* (*E. coli*, ATCC 27195) and Gram-positive *Staphylococcus aureus* (*S. aureus*, ATCC 25923) using a previously reported method.[48] Briefly, single colonies of *E. coli* and *S. aureus* were inoculated into 10 mL of sterile liquid Muller–Hinton (MH) broth medium (Sigma-Aldrich St Louis, MO, United States).[82] After that, 1.5×10^6 CFU mL^{-1} of bacteria was prepared by diluting the bacterial suspension with sterile PBS (0.01 mM, pH 7.4). The bacterial suspension was then treated differently on agar plates: (a) bacteria alone; (b) bacteria + P8PVA3; (c) bacteria + P8PVA3-TA. All the tested bacterial species were incubated at 37 °C for 24 h.[83] After 24 h of incubation, the bacteria colonies grown on the agar plates were photographed.

Scanning electron microscopy. To investigate the surface topography and porosity, different hydrogels samples were examined by SEM (FEI Quanta 200 FEG). The freeze-dried samples were first cross-sectioned and coated with platinum before the SEM observations.[84]

X-Ray computed microtomography (Micro-CT) analysis. The hydrogels were scanned with a micro-CT scanner (NEOSCAN N80, Mechelen, Belgium) to investigate the porosity and pore size of the 3D structure. The scanned images were acquired by scanning the scaffolds at 50 kV, 80 μA, with an image pixel size of 2.0 μm, rotation step of 0.2°, and averaging (Nframes) of 8 frames without a filter. The scanned images were further reconstructed by adjusting the parameters of misalignment correction and beam hardening at −10.0 and 20 pixels, respectively, with a ring correction of 10 and beam hardening of 20%, which were then 3D visualized using the software. To measure the porosity and pore size of the samples, object analysis was performed on 3 different single slices within the volume of interest (VOI). The analysis results are the average of the obtained data from 3 single slices of each sample.

Digestion of the samples by Galleria mellonella larvae and histopathological examination of larval tissue. *G. mellonella* larvae were reared at 30 °C in darkness. Sixth-instar larvae, each weighing 0.2 ± 0.02 g, were selected for the experiments. Each sample type was sectioned and weighed; an approximately 0.05 g piece was introduced to an individual larva and incubated for 168 h. The sample was weighed every 24 h. Subsequently, the larvae were fixed in 2% formaldehyde and subjected to histopathological examination using standard hematoxylin and eosin (H&E) staining. A total of nine larvae were used for this experiment.

Cytotoxicity of locally applied samples on *G. mellonella* larvae. Sixth-instar larvae, each weighing 0.2 ± 0.02 g, were selected for the experiments. The larvae were embedded within the samples. In addition to P8PVA3, P8PVA3-B, and P8PVA3-TA, a usability control (sterile cotton material soaked with the pesticide permethrin) and a growth control (sterile cotton material soaked with saline) were employed. Nine larvae per group were used, totaling 45 larvae for this experiment. The experiment was conducted over 168 h, with the daily monitoring of larval mortality. Death was defined by immobility, melanization, and a lack of response to physical stimuli.

4.4 Statistical analysis

Data are shown as the mean ± standard deviation (SD), with the number of independent samples (*n*) indicated in the figure captions. Given the small sample sizes in this study, non-parametric statistical methods were used to ensure the robustness of the analysis without reliance on normality assumptions. The Kruskal–Wallis test was employed for comparisons between groups in the mechanical tests (compressive modulus, toughness, and number of compression cycles), followed by Dunn–Sidak's test for the *post-hoc* pairwise comparisons. For the cell viability results, the timepoint was treated as an independent factor, and the Kruskal–Wallis test was used for group comparisons, with the significance level reported in the figure captions. In-depth pairwise comparisons for cell viability were not performed due to the limited statistical power. All the statistical analyses were performed using Origin Pro 2021.

Author contributions

Conceptualization: J.S.S, P.H, A.S. Data curation: J.S.S, P.H., P.G, M.L. Formal analysis: J.S.S, P.H., P.G, H.J, M.L. Investigation: J.S.S, P.H., P.G, H.J., A.J. Methodology: J.S.S, P.H., P.G, H.J., A.S, A.J. Project administration: A.S, Resources: A.S. Supervision: A.S. Validation: A.S, L.N. Visualization: J.S.S, P.H. Writing – original draft: J.S.S, P.H, P.G, M.L, A.J. Writing – review & editing: J.S.S, P.H., P.G, H.J, M.L, A.S, L.N, C.D., A.J.

All authors have read and agreed to the published version of the manuscript.

Data availability

The data supporting this article have been included as part of the ESI.†

Conflicts of interest

The authors declare no conflict of interest.

Acknowledgements

This study was supported by an Aspirant fellowship from the Fonds National de la Recherche Scientific de Belgique (FNRS) (grant number 46599, 2022, awarded to Julia Simińska-Stanny and grant number 38351, 2021, awarded to Pejman Ghaffari-Bohlouli). Armin Shavandi acknowledges the support of FNRS CDR J.0188.24. The graphical abstract and Fig. 1A, C, 2A, 3A–C and 6E were created using BioRender.com.

J. S. S. and P. G. B. gratefully acknowledge the support by a grant from the FNRS (J. S. S. FNRS-Aspirant, Grant No. FC 46599, P.G.B. No. FC 38351). M. L. acknowledges the China Scholarship Council for the PhD scholarship (Grant No. 202308410182). Some of the equipment used in this study is financed in whole or in part by the Walloon Region (Technology Platforms of Excellence 'Alternative to animal experimentation' and 'Biogreen').

We would like to acknowledge Chen Li, Ioanna Skiadas, Thibault Vanderbeken and Daniel Sadat, who helped with resin characterizations.

References

1 Z. Guo, *et al.*, An effective DLP 3D printing strategy of high strength and toughness cellulose hydrogel towards strain sensing, *Carbohydr. Polym.*, 2023, **315**, 121006.
2 S. Rouf, *et al.*, Additive manufacturing technologies: Industrial and medical applications, *Sustainable Oper. Comput.*, 2022, **3**, 258–274.
3 G. Zhu, *et al.*, Digital Light Processing 3D Printing of Healable and Recyclable Polymers with Tailorable Mechanical Properties, *ACS Appl. Mater. Interfaces*, 2021, **13**(29), 34954–34961.
4 R. Levato, *et al.*, High-resolution lithographic biofabrication of hydrogels with complex microchannels from low-temperature-soluble gelatin bioresins, *Mater. Today Bio*, 2021, **12**, 100162.
5 M. Hakim Khalili, *et al.*, Mechanical Behavior of 3D Printed Poly(ethylene glycol) Diacrylate Hydrogels in Hydrated Conditions Investigated Using Atomic Force Microscopy, *ACS Appl. Polym. Mater.*, 2023, **5**(4), 3034–3042.
6 S. Kumari, P. Mondal and K. Chatterjee, Digital light processing-based 3D bioprinting of κ-carrageenan hydrogels for engineering cell-loaded tissue scaffolds, *Carbohydr. Polym.*, 2022, **290**, 119508.
7 W. Jia, *et al.*, A multicrosslinked network composite hydrogel scaffold based on DLP photocuring printing for nasal cartilage repair, *Biotechnol. Bioeng.*, 2024, **121**(09), 2752–2766.
8 J. H. Galarraga, *et al.*, Synthesis, Characterization, and Digital Light Processing of a Hydrolytically Degradable Hyaluronic Acid Hydrogel, *Biomacromolecules*, 2023, **24**(1), 413–425.
9 P. Song, *et al.*, DLP fabricating of precision GelMA/HAp porous composite scaffold for bone tissue engineering application, *Composites, Part B*, 2022, **244**, 110163.
10 W. Ye, *et al.*, 3D printing of gelatin methacrylate-based nerve guidance conduits with multiple channels, *Mater. Des.*, 2020, **192**, 108757.
11 S. H. Kim, *et al.*, 4D-bioprinted silk hydrogels for tissue engineering, *Biomaterials*, 2020, **260**, 120281.
12 H. Li, *et al.*, Digital light processing (DLP)-based (bio)printing strategies for tissue modeling and regeneration, *Aggregate*, 2023, **4**(2), e270.
13 M. Hakim Khalili, *et al.* Additive Manufacturing and Physicomechanical Characteristics of PEGDA Hydrogels: Recent Advances and Perspective for Tissue Engineering, *Polymers*, 2023, **15**(10), 2341.
14 J. Simińska-Stanny, *et al.*, Advanced PEG-tyramine biomaterial ink for precision engineering of perfusable and flexible small-diameter vascular constructs via coaxial printing, *Bioact. Mater.*, 2024, **36**, 168–184.
15 H. Goodarzi Hosseinabadi, *et al.*, Ink material selection and optical design considerations in DLP 3D printing, *Appl. Mater. Today*, 2023, **30**, 101721.
16 X. Qin, *et al.*, Methacrylated pullulan/polyethylene (glycol) diacrylate composite hydrogel for cartilage tissue engineering, *J. Biomater. Sci., Polym. Ed.*, 2021, **32**(8), 1057–1071.

17 Q. Hu, *et al.*, 3D Printing GelMA/PVA Interpenetrating Polymer Networks Scaffolds Mediated with CuO Nanoparticles for Angiogenesis, *Macromol. Biosci.*, 2022, **22**(10), 2200208.

18 C. Wang, *et al.*, Facile fabrication and characterization of high-performance Borax-PVA hydrogel, *J. Sol-Gel Sci. Technol.*, 2022, **101**(1), 103–113.

19 M. Huang, *et al.*, High performances of dual network PVA hydrogel modified by PVP using borax as the structure-forming accelerator, *Des. Monomers Polym.*, 2017, **20**(1), 505–513.

20 M. Caprioli, *et al.*, 3D-printed self-healing hydrogels via Digital Light Processing, *Nat. Commun.*, 2021, **12**(1), 2462.

21 N. R. Richbourg, *et al.*, Precise control of synthetic hydrogel network structure via linear, independent synthesis-swelling relationships, *Sci. Adv.*, 2021, **7**(7), eabe3245.

22 J. Zheng, *et al.*, Self-healing polymer design from dynamic B–O bonds to their emerging applications, *Mater. Chem. Front.*, 2023, **7**(3), 381–404.

23 G. He, *et al.*, Preparation of poly (vinyl alcohol)/polydopamine/tannin acid composite hydrogels with dual adhesive, antioxidant and antibacterial properties, *Eur. Polym. J.*, 2024, **205**, 112708.

24 Y.-N. Chen, *et al.*, Poly (vinyl alcohol)–tannic acid hydrogels with excellent mechanical properties and shape memory behaviors, *ACS Appl. Mater. Interfaces*, 2016, **8**(40), 27199–27206.

25 K. Chen, *et al.*, An all-in-one tannic acid-containing hydrogel adhesive with high toughness, notch insensitivity, self-healability, tailorable topography, and strong, instant, and on-demand underwater adhesion, *ACS Appl. Mater. Interfaces*, 2021, **13**(8), 9748–9761.

26 S. Adel Rashiq, *et al.*, Enhanced Bioadhesive and Antimicrobial Properties of PVA/Ascorbic Acid Composite with Tannic Acid Synthesized by Gamma Irradiation for Biomedical Applications, *ACS Omega*, 2025, **10**(14), 13839–13853.

27 A. Bigham, *et al.*, Advances in tannic acid-incorporated biomaterials: Infection treatment, regenerative medicine, cancer therapy, and biosensing, *Chem. Eng. J.*, 2022, **432**, 134146.

28 P. Hobbi, *et al.*, Fabrication of bioactive polyphenolic biomaterials for bone tissue engineering, *Mater. Today Sustainability*, 2023, **24**, 100541.

29 M. Kumar, *et al.*, Tribo-mechanical and biological characterization of PEGDA/bioceramics composites fabricated using stereolithography, *J. Manuf. Processes*, 2022, **77**, 301–312.

30 H. Hu, *et al.*, PVA/PEGDA microgels loaded with L-cysteine for corrosion inhibition coating on fragile bronze, *J. Coat. Technol. Res.*, 2024, **22**(02), 631–649.

31 K. Wu, *et al.*, 3D Printed Silk Fibroin-Based Hydrogels with Tunable Adhesion and Stretchability for Wearable Sensing, *Adv. Funct. Mater.*, 2024, 2404451.

32 T. Kuhnt, *et al.*, An efficient and easily adjustable heating stage for digital light processing set-ups, *Addit. Manuf.*, 2021, **46**, 102102.

33 P. Sokola, *et al.*, Kinetic stability and rheological properties of photosensitive zirconia suspensions for DLP printing, *Ceram. Int.*, 2023, **49**(11, Part B), 18502–18509.

34 Y. Li, *et al.*, High-fidelity and high-efficiency additive manufacturing using tunable pre-curing digital light processing, *Addit. Manuf.*, 2019, **30**, 100889.

35 B. He, *et al.*, 3D printed biomimetic epithelium/stroma bilayer hydrogel implant for corneal regeneration, *Bioact. Mater.*, 2022, **17**, 234–247.

36 Y. Wang, *et al.*, Dimethyl sulfoxide mediated high-fidelity 3D printing of hydrogels, *Addit. Manuf.*, 2024, **91**, 104346.

37 A. Alafnan, *et al.*, Development and characterization of PEGDA microneedles for localized drug delivery of gemcitabine to treat inflammatory breast cancer, *Materials*, 2022, **15**(21), 7693.

38 J. Li, *et al.*, Facile microfluidic synthesis of copolymer hydrogel beads for the removal of heavy metal ions, *J. Mater. Sci.*, 2016, **51**, 10375–10385.

39 A. R. Jamali, A. A. Shaikh and A. D. Chandio, *Enhancing the flexibility of PVA membrane through glycerol addition*. 2023.

40 E. Al-Emam, *et al.*, Characterization of polyvinyl alcohol-borax/agarose (PVA-B/AG) double network hydrogel utilized for the cleaning of works of art, *Heritage Sci.*, 2020, **8**, 1–14.

41 H. Ochiai, *et al.*, Mechanical and thermal properties of poly (vinyl alcohol) crosslinked by borax, *Polym. J.*, 1976, **8**(1), 131–133.

42 C. Wang, *et al.*, Facile fabrication and characterization of high-performance Borax-PVA hydrogel, *J. Sol-Gel Sci. Technol.*, 2022, 1–11.

43 M. Liao, *et al.*, A good adhesion and antibacterial double-network composite hydrogel from PVA, sodium alginate and tannic acid by chemical and physical cross-linking for wound dressings, *J. Mater. Sci.*, 2023, **58**(13), 5756–5772.

44 Q. Yao, *et al.*, Tannic acid/polyvinyl alcohol/2-hydroxypropyl trimethyl ammonium chloride chitosan double-network hydrogel with adhesive, antibacterial and biocompatible properties, *React. Funct. Polym.*, 2022, **179**, 105384.

45 D. Lee, *et al.*, VATA: a poly (vinyl alcohol)-and tannic acid-based nontoxic underwater adhesive, *ACS Appl. Mater. Interfaces*, 2020, **12**(18), 20933–20941.

46 J. Simińska-Stanny, *et al.*, Optimizing phenol-modified hyaluronic acid for designing shape-maintaining biofabricated hydrogel scaffolds in soft tissue engineering, *Int. J. Biol. Macromol.*, 2023, **244**, 125201.

47 T. Şener Raman, *et al.*, A study on the material properties of novel PEGDA/gelatin hybrid hydrogels polymerized by electron beam irradiation, *Front. Chem.*, 2022, **10**, 1094981.

48 H. Jafari, *et al.*, Tannic acid post-treatment of enzymatically crosslinked chitosan-alginate hydrogels for biomedical applications, *Carbohydr. Polym.*, 2022, **295**, 119844.

49 D. Chawla, *et al.*, 3D bioprinted alginate-gelatin based scaffolds for soft tissue engineering, *Int. J. Biol. Macromol.*, 2020, **144**, 560–567.

50 A. Rozmysłowska-Wojciechowska, *et al.* Controlling the Porosity and Biocidal Properties of the Chitosan-Hyaluronate Matrix Hydrogel Nanocomposites by the Addition of 2D Ti3C2Tx MXene, *Materials*, 2020, **13**(20), 4587, DOI: **10.3390/ma13204587**.

51 I. C. Carvalho and H. S. Mansur, Engineered 3D-scaffolds of photocrosslinked chitosan-gelatin hydrogel hybrids for

chronic wound dressings and regeneration, *Mater. Sci. Eng., C*, 2017, **78**, 690–705.
52 T. E. L. Douglas, *et al.*, Enrichment of chitosan hydrogels with perfluorodecalin promotes gelation and stem cell vitality, *Mater. Lett.*, 2014, **128**, 79–84.
53 J. Lee and G. Kim, Calcium-deficient hydroxyapatite/collagen/platelet-rich plasma scaffold with controlled release function for hard tissue regeneration, *ACS Biomater. Sci. Eng.*, 2018, **4**(1), 278–289.
54 D. George, K. M. S. Begum and P. U. Maheswari, Sugarcane bagasse (SCB) based pristine cellulose hydrogel for delivery of grape pomace polyphenol drug, *Waste Biomass Valorization*, 2020, **11**, 851–860.
55 M. Tangarfa, N. Semlali Aouragh Hassani and A. Alaoui, Behavior and Mechanism of Tannic Acid Adsorption on the Calcite Surface: Isothermal, Kinetic, and Thermodynamic Studies, *ACS Omega*, 2019, **4**(22), 19647–19654.
56 T. Thanyacharoen, *et al.*, Development of a gallic acid-loaded chitosan and polyvinyl alcohol hydrogel composite: Release characteristics and antioxidant activity, *Int. J. Biol. Macromol.*, 2018, **107**, 363–370.
57 H. A. Merchant, *et al.*, Once-daily tablet formulation and in vitro release evaluation of cefpodoxime using hydroxypropyl methylcellulose: a technical note, *AAPS PharmSciTech*, 2006, **7**, E178–E183.
58 E. Lenzi, *et al.*, Diffusion processes and drug release: Capsaicinoids-loaded poly (ε-caprolactone) microparticles, *PLoS One*, 2016, **11**(6), e0157662.
59 R. T. P. Upputuri and A. K. A. Mandal, Mathematical modeling and release kinetics of green tea polyphenols released from casein nanoparticles, *Iran. J. Pharm. Res.*, 2019, **18**(3), 1137.
60 D. Ciolacu, *et al.*, New cellulose–lignin hydrogels and their application in controlled release of polyphenols, *Mater. Sci. Eng., C*, 2012, **32**(3), 452–463.
61 H. Jafari, *et al.*, Tissue adhesive hydrogel based on upcycled proteins and plant polyphenols for enhanced wound healing, *Mater. Today Chem.*, 2023, **33**, 101722.
62 F. Azadikhah and A. R. Karimi, Injectable photosensitizing supramolecular hydrogels: A robust physically cross-linked system based on polyvinyl alcohol/chitosan/tannic acid with self-healing and antioxidant properties, *React. Funct. Polym.*, 2022, **173**, 105212.
63 K. H. Hong, Polyvinyl alcohol/tannic acid hydrogel prepared by a freeze-thawing process for wound dressing applications, *Polym. Bull.*, 2017, **74**(7), 2861–2872.
64 İ. Gülçin, *et al.*, Radical scavenging and antioxidant activity of tannic acid, *Arabian J. Chem.*, 2010, **3**(1), 43–53.
65 X. Huang, *et al.*, A NIR-II light-modulated injectable self-healing hydrogel for synergistic photothermal/chemodynamic/chemo-therapy of melanoma and wound healing promotion, *J. Mater. Chem. B*, 2022, **10**(38), 7717–7731.
66 B. Kaczmarek, Tannic Acid with Antiviral and Antibacterial Activity as A Promising Component of Biomaterials—A Minireview, *Materials*, 2020, **13**(14), 3224, DOI: **10.3390/ma13143224**.
67 G. Tripodo, *et al.*, Hydrogels for biomedical applications from glycol chitosan and PEG diglycidyl ether exhibit pro-angiogenic and antibacterial activity, *Carbohydr. Polym.*, 2018, **198**, 124–130.
68 L. Huang, *et al.*, Silver doped-silica nanoparticles reinforced poly (ethylene glycol) diacrylate/hyaluronic acid hydrogel dressings for synergistically accelerating bacterial-infected wound healing, *Carbohydr. Polym.*, 2023, **304**, 120450.
69 L. Antonini, *et al.*, Osteogenic differentiation of bone marrow-derived mesenchymal stem cells on anodized niobium surface, *J. Mater. Sci.: Mater. Med.*, 2019, **30**(104), 1–13.
70 P. Mogha, S. Iyer and A. Majumder, Extracellular matrix protein gelatin provides higher expansion, reduces size heterogeneity, and maintains cell stiffness in a long-term culture of mesenchymal stem cells, *Tissue Cell*, 2023, **80**, 101969.
71 P. T. J. Hwang, *et al.*, Endothelium-Mimicking Nanomatrix Coating to Enhance Endothelialization after Left Atrial Appendage Closure Device Implantation, *ACS Appl. Bio Mater.*, 2021, **4**(6), 4917–4924.
72 I. Serrano, *et al.*, The Virtuous Galleria mellonella Model for Scientific Experimentation, *Antibiotics*, 2023, **12**(3), 505.
73 D. Debroy, J. Oakey and D. Li, Interfacially-mediated oxygen inhibition for precise and continuous poly(ethylene glycol) diacrylate (PEGDA) particle fabrication, *J. Colloid Interface Sci.*, 2018, **510**, 334–344.
74 S. Petit and J. Madejova, Chapter 2.7 - Fourier Transform Infrared Spectroscopy, in *Developments in Clay Science*, ed. F. Bergaya and G. Lagaly, Elsevier, 2013, pp. 213–231.
75 N. M. Hapipi, *et al.*, The Rheological Studies on Poly(vinyl) Alcohol-Based Hydrogel Magnetorheological Plastomer, *Polymers*, 2020, **12**(10), 2332.
76 J. Liu, *et al.*, Additive-lathe 3D bioprinting of bilayered nerve conduits incorporated with supportive cells, *Bioact. Mater.*, 2021, **6**, 219–229.
77 L. A. Al-Zube, *et al.*, Measuring the compressive modulus of elasticity of pith-filled plant stems, *Plant Methods*, 2017, **13**(1), 99.
78 L. Chang, *et al.*, Hyaluronic acid methacrylate/laponite hydrogel loaded with BMP4 and maintaining its bioactivity for scar-free wound healing, *Regener. Biomater.*, 2023, **10**, rbad023.
79 R. Sesia, *et al.* UV-Cured Chitosan-Based Hydrogels Strengthened by Tannic Acid for the Removal of Copper Ions from Water, *Polymers*, 2022, **14**(21), 4645, DOI: **10.3390/polym14214645**.
80 A. M. Rahimi, M. Cai and S. Hoyer-Fender, Heterogeneity of the NIH3T3 Fibroblast Cell Line, *Cells*, 2022, **11**(17), 2677.
81 G.-Z. Jin and H.-W. Kim, Efficacy of collagen and alginate hydrogels for the prevention of rat chondrocyte dedifferentiation, *J. Tissue Eng.*, 2018, **9**, 204173141880243.
82 D. Li, *et al.*, Synergistical Starvation and Chemo-Dynamic Therapy for Combating Multidrug-Resistant Bacteria and Accelerating Diabetic Wound Healing, *Adv. Healthcare Mater.*, 2021, **10**(18), e2100716.

83 X. Qin, *et al.*, Metal-Phenolic Nanocapsules with Photothermal Antibacterial and Ros Scavenging Ability for Diabetic Wound Healing, *Adv. Healthcare Mater.*, 2024, **13**(10), e2303604.

84 A. Shavandi, *et al.*, Biomaterial ink based on bacterial polyglucuronic acid for tissue engineering applications, *Next Materials*, 2024, **4**, 100181.